Influence of finite size and surface effects on the structural, electrical and magnetic properties of nanostructured nickel oxide

P. A. Sheena[1,2] · H. Hitha[3] · A. Sreedevi[3] · Thomas Varghese[3]

Abstract

A detailed study on the influence of crystallite size variation on the structural, electrical and magnetic properties of nickel oxide nanoparticles is reported here. The characterization techniques reveal the structural modification of the samples which resulted from the variation in crystallite size. The grain boundaries and triple junctions in the interfacial regions play a pivotal role in deciding the transport properties of nanocrystalline NiO. The dielectric measurements confirm high value of dielectric constant for NiO nanoparticles at low frequency, which can be used for the fabrication of gate dielectric in metal oxide semiconductor field effect transistors. The superparamagnetic behaviour of samples with a size ~ 8 nm points out the significance of surface atoms and uncompensated surface spins. The results highlight the role of finite size and surface effects in determining the properties of nanostructured nickel oxide.

1 Introduction

Nanomaterials usually exhibit unique properties that are technologically important and strongly different from those of their bulk counterparts [1]. Owing to the extremely small dimensions of nanostructured materials, most of the atoms lie at or near the surface, and the surface and interface effects become more significant [2]. Due to the surface modification caused by microstructural defects, the electrical properties of nanoparticles show a large deviation from those of their single crystal and polycrystalline counterparts. Surface and finite size effects induce anomalous behaviour in their magnetic properties also [3].

Nanosized transition metal oxides have gained much attention due to their abnormal physical properties induced by the small size and surface effects [4–6]. Among them, nickel oxide (NiO) is a promising material extensively used in various fields, such as magnetic materials, catalysis, gas sensors, electrochromic films, lithium-ion batteries and electrochemical capacitors [7–12]. Bulk NiO is classified as a Mott–Hubbard insulator having apparent room temperature electrical conductivity of 10^{-9}–10^{-11}ohm^{-1} m^{-1} [13]. The conductivity of nanocrystalline NiO is drastically increased due to the surface modification caused by microstructural defects such as nickel vacancies and interstitial oxygen in NiO crystallites [14, 15]. For size less than 10 nm, the interfacial region composed of grain boundaries and triple junctions decide the transport properties of NiO nanoparticles [16, 17]. The magnetic properties of NiO nanoparticles are sensitive to size, crystal structure, and morphology. Bulk NiO is an antiferromagnetic material with a Neel temperature of 523 K and can be used in spin valves and magnetic tunnel junctions [18]. Reduction in particle size can cause disturbance in the magnetic structure of NiO. Neel suggested that nanoparticles with the antiferromagnetic ordering of spin exhibit superparamagnetism and weak ferromagnetism [19]. As the surface to volume ratio becomes sufficiently large, the particles can have a nonzero net magnetic moment due to uncompensated surface spins [20]. The significance of inter-particle interaction in analysing the magnetic properties of NiO nanoparticles is reported by Bodker et al. [21]. Khadar et al. reported a transition from superparamagnetic to super-antiferromagnetic state with an increase in crystallite size of nanocrystalline NiO [22].

To explore the size and surface effects on the crystal structure and properties of nanophase NiO, nanoparticles with different sizes are grown by calcining the precursor

✉ Thomas Varghese
nanoncm@gmail.com

1 Department of Physics, M.E.S. Asmabi College, P. Vemballur, Kerala 680 671, India

2 Department of Physics, Newman College, Thodupuzha, Kerala 685584, India

3 Dept. of Physics, Nanoscience Research Centre (NSRC), Nirmala College, Muvattupuzha, Kerala 686 661, India

synthesized by chemical precipitation method at different temperatures. The calcined NiO samples characterized by X-ray diffraction (XRD) and high-resolution transmission electron microscopy (HRTEM) techniques reveal the structural modification resulted from the variation in crystallite size. The electrical properties of the NiO samples are examined by measuring DC and AC conductivities and dielectric properties. The magnetic properties of the NiO samples are investigated using vibrating sample magnetometre (VSM). The results of the present study constitute the first report for the detailed investigation on the influence of finite size and surface effects in determining the properties of nanostructured nickel oxide.

2 Materials and methods

2.1 Synthesis

Nickel nitrate hexahydrate ($Ni(NO_3)_2 \cdot 6H_2O$) (99.8%, Merck) and ammonium carbonate ($(NH_4)_2CO_3$) (99.9%, Merck) are used for the synthesis. Nanocrystalline NiO samples are prepared by reacting aqueous solutions of nickel nitrate hexahydrate and ammonium carbonate (0.1 M each). The reactants are mixed at room temperature under magnetic stirring. The precipitate is allowed to settle down overnight and is collected by the decantation of the supernatant liquid. It is then washed with distilled water several times to remove the unreacted salts and impurities. Finally, the precipitate is filtered and dried in a hot-air oven at 70 °C for 18 h. The precursor obtained is ground into a fine powder using mortar and pestle. The powder is then calcined in a muffle furnace at 400, 500 and 600 °C for 3 h. The calcined NiO samples at 400, 500 and 600 °C are denoted as N0, N1 and N2, respectively.

2.2 Characterization

The thermal stability of the precursor is studied using thermogravimetric and differential thermal analysis techniques (TGA/DTA) (Perkin Elmer STA 6000, at a heating rate of 10 °C min^{-1}). The structural characterization of the samples are done using X-ray diffraction (XRD) (Bruker D8 advance with CuK$_\alpha$ = 1.5406 Å radiation) and high-resolution transmission electron microscope (HRTEM) (Jeol JEM 2100 accelerated by 200 kV).

DC conductivity of the samples is recorded using *KEITHLEY 2450 Source Meter* in two-probe method in the temperature range 30–150 °C. Dielectric behaviour of the samples is studied using a computer-controlled frequency response analyzer (HIOKI LCR HI tester, model: 3532) as a function of frequency (50 Hz–5 MHz) at selected temperatures. For electrical studies, the samples are consolidated in the form of cylindrical pellets of diametre 13 mm and thickness 1.5 mm using a hydraulic press at a pressure of 7 GPa. The prepared pellets are then sintered at 400 °C for 2 h. Both faces of the pellets are coated with air-drying silver paste for good electrical contact.

Magnetic measurements are carried out using vibrating sample magnetometre (VSM) (Lakeshore VSM 7410) with a maximum magnetic field of 15 kOe for all the samples at room temperature (300 K).

3 Results and discussion

3.1 Thermal analysis

The TGA/DTA and DTG curves of the precursor are shown in Fig. 1. The TGA curve indicates an appreciable weight loss of the precursor from 50 to 350 °C. This suggests a complete decomposition of the precursor at 350 °C to become nickel oxide [23]. The first weight loss peak located around 100 °C indicates the thermal dehydration of the precursor and the evaporation of physically adsorbed impurities. The second peak and the endothermic peak indicated by DTA near 300 °C may be related to the decomposition of nickel carbonate into nickel oxide and carbon dioxide [24, 25]. Based on the results of TGA, a temperature of 400 °C was chosen to ensure the complete decomposition of the precursor to form nickel oxide.

3.2 Structural analysis

3.2.1 Powder XRD

Figure 2 shows the XRD patterns of as-synthesized and calcined samples. Well-defined diffraction peaks with preferential orientation along the (200) planes are observed for all the samples, which confirm their crystalline nature. The peaks corresponding to (111), (200), (220), (311) and (222) planes can be indexed to face-centred cubic bunsenite
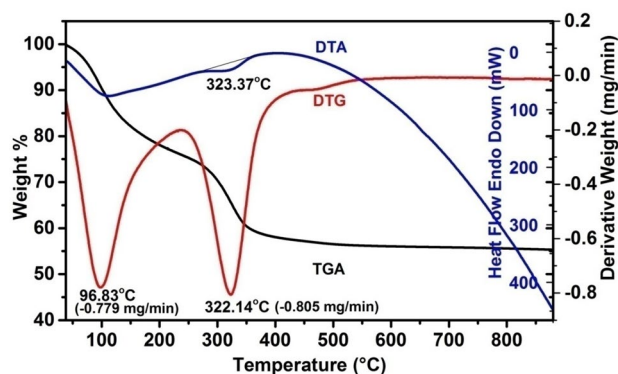
Fig. 1 TGA/DTA/DTG curves of the precursor
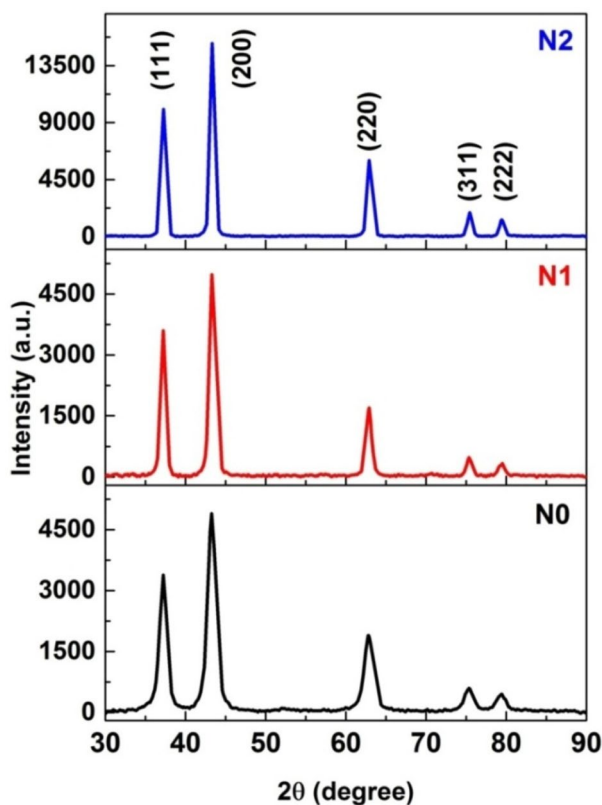
Fig. 2 XRD patterns of N0, N1 and N2

structure (space group: *Fm3m*) of NiO [23], which is in agreement with the standard spectrum (JCPDS No.73-1519). The absence of additional peaks in the pattern indicates the phase purity of the sample. The peaks get sharper and more intense with an increase in calcination temperature, indicating an increase in crystallite size and a better crystal quality [26].

The average crystallite sizes calculated using Scherrer equation [27] are 8.2, 12.4 and 18.5 nm, respectively, for N0, N1 and N2 samples. This size can be smaller than the actual value, as the lattice defects and strain can have an effect on the XRD peaks [28]. Hence the effect of crystallite size and lattice strain on the full width at half maximum (FWHM) of XRD peaks has been studied using the Williamson–Hall (W–H) method [29]. W–H plots for the nickel oxide samples are shown in Fig. 3. The points are getting closer towards its linear fit with an increase in calcination temperature, which confirms the increase in crystallinity of NiO nanoparticles.

The geometric parameters of the samples calculated from XRD data are tabulated in Table 1. The decrease in FWHM with the increase in calcination temperature is an indication of increased crystallite size. Due to the decrease in interplanar spacing XRD peaks shift to higher 2θ values upon calcination. The lattice constant (*a*) of the samples estimated from the spacing of the (200) lattice
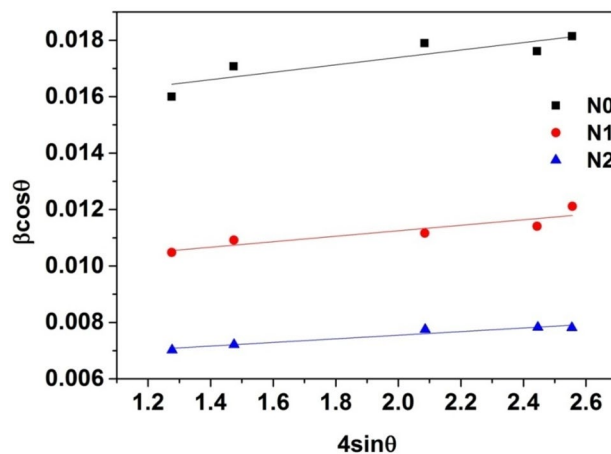
Fig. 3 W–H plots of NiO nanoparticles

planes and the unit cell volume ($V = a^3$) is presented in the table. These results match with the values given in the XRD pattern of JCPDS Card No. 73-1519 for NiO. It can be seen from Table 1 that calcination leads to a decrease in lattice constant and hence to lattice contraction. The decrease in micro-strain with the increase in crystallite size is also observed, which indicates that defects such as dislocations, edges or cuts are removed during calcination [30].

3.2.2 HRTEM

The bright-field image, HRTEM image and selected area diffraction (SAED) patterns of N0, N1 and N2, respectively, are displayed in Fig. 4. The bright-field (BF) images of the samples show a large number of particles with a hexagonal shape. The particle growth upon calcination is evident from the BF images. The unidirectional fringe patterns are clearly observed for all the samples from HRTEM images. The clear diffraction spots in the SAED patterns confirm the crystalline nature of all the samples. The average particle size obtained from TEM images is shown in Table 2. The spacing between the successive planes for the three prominent peaks is calculated from the SAED patterns and is tabulated. The large size for N2 indicates aggregation of grains upon calcination (Table 3).

3.3 Electrical properties

3.3.1 DC conductivity

The variation in DC conductivity (σ_{dc}) over the temperature range of 313–423 K for the samples N0, N1 and N2 is shown in Fig. 5. The increase in electrical conductivity with temperature shows the semiconducting behaviour of all the

Table 1 Geometric parameters of N0, N1 and N2

Sample	Average crystallite size (nm)		FWHM (200) plane	2θ ((200) peak)	Lattice spacing d_{200} (Å)	Lattice constant a (Å)	Unit cell volume (Å³)	Micro-strain ($\times 10^{-4}$)
	Scherrer method	W–H method						
JCPDS Card No. 73-1519	–	–	–	43.253°	2.0900	4.168	72.43	–
N0	8.2 ± 0.164	9.3 ± 0.186	0.968°	43.259°	2.0897	4.179	73.003	13.110
N1	12.4 ± 0.248	14.7 ± 0.297	0.673°	43.276°	2.0889	4.178	72.930	9.718
N2	18.5 ± 0.370	21.9 ± 0.438	0.445°	43.301°	2.0876	4.175	72.773	6.397
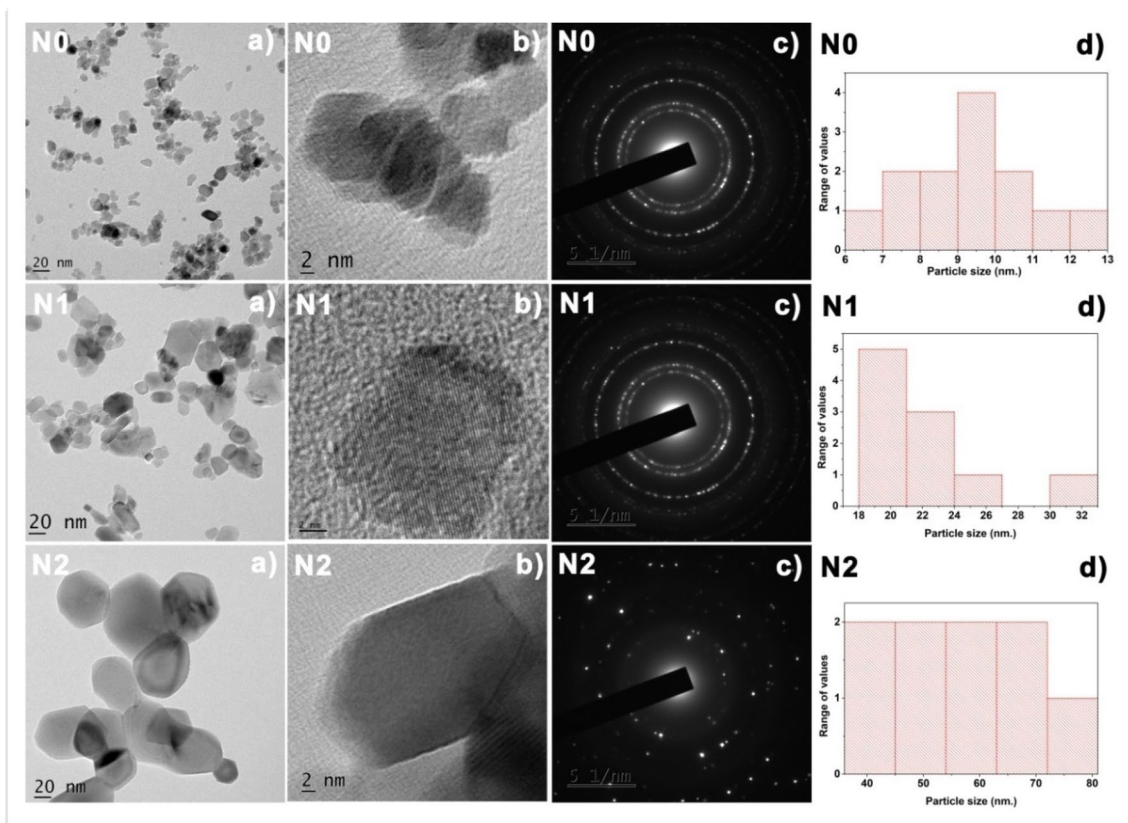
Fig. 4 **a** Bright-field images, **b** HRTEM images, **c** SAED patterns and **d** particle size distribution of N0, N1 and N2

Table 2 Geometrical parameters of the samples from TEM images

Sample	Particle size from TEM images (nm)	d spacing from SAED patterns (nm)		
		(111)	(200)	(220)
N0	11.4 ± 0.228	0.2856	0.2463	0.1745
N1	21.8 ± 0.256	0.2786	0.2472	0.1718
N2	57 ± 1.14	0.2656	0.2406	0.1609

samples. The charge carriers are thermally activated with an increase in temperature, which increases their drift mobility and hence the conductivity.

The DC conductivities of all samples are much higher than that of NiO single crystals having apparent room temperature conductivity of 10^{-9}–10^{-11}ohm^{-1} m^{-1} [31]. The enhanced conductivity in NiO nanoparticles is due to the presence of a large number of Ni^{2+} vacancies on the surface [32]. The band structure of NiO consists of multiple valence band made up of a 3d band of Ni^{2+} and 2p band of O^{2-} and conduction band with a 4s band of Ni^{2+} and the 3s band of O^{2-}. The Ni^{2+} vacancies in the sample correspond to an acceptor-like level in the energy gap close to the Fermi level just above the localized 3d band of Ni^{2+} and the wide 2p band of O^{2-}. These vacancies result in the transformation of two adjacent Ni^{2+} ions into Ni^{3+} ions to

Table 3 Equivalent circuit parameters of N0, N1 and N2 samples

Sample	L_S (H)	CPE_g (F)	R_g (Ω)	β_g	CPE_{gb} (F)	R_{gb} (Ω)	β_{gb}
N0	2.353E−06	1.422E−10	359.11	0.9652	2.702E−08	709.18	0.7741
N1	2.103E−06	1.290E−10	195.15	0.9910	3.401E−08	238.89	0.7974
N2	2.182E−06	1.319E−08	723.61	0.6959	1.875E−08	5812.7	0.8210
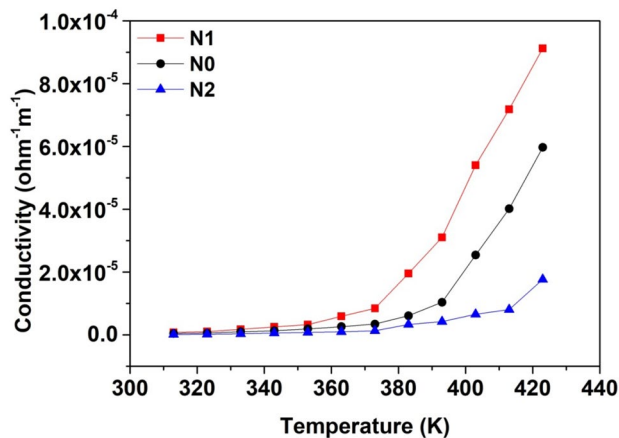
Fig. 5 Variation in DC conductivity with temperature for N0, N1 and N2

Fig. 6 Variation of dielectric constant with frequency for samples N0, N1 and N2 at 303 K

acquire charge neutrality and cause distortion in the lattice [14, 16]. The created Ni^{3+} ions donate a hole into the lattice. If a 3d electron from an adjacent Ni^{2+} ion is transferred to a Ni^{3+} ion, a hole is created in the 3d band. This hole along with the associated lattice distortion creates a small polaron in the localized 3d band of Ni^{2+}. A hole is also created in the 2p band of O^{2-} ion when a 2p electron is transferred from a nearby O^{2-} ion to the Ni^{3+} ion. The hole and the associated lattice distortion constitute a large polaron in the 2p band of O^{2-} [16]. As the number of Ni^{2+} vacancies in the sample increases, the number of small polarons in the localized 3d band of Ni^{2+} and the large polarons in the 2p band of O^{2-} increase, which enhances the conductivity [14, 16].

The conductivity is found to increase and then decrease with increase in particle size from 8.2 to 18.5 nm. The result indicates the finite-size effect on the variation in DC conductivity of nanocrystalline NiO. In nanocrystalline materials with crystallite size less than 10 nm, the interfacial region composed of grain boundaries and triple junctions has an important role in deciding its transport properties [33, 34]. Triple junctions which are intersection lines of three or more adjoining crystallites can be viewed as line defects. Unlike grain boundaries, triple junctions act as a potential barrier, causing scattering of charge carriers and hence decrease in conductivity [17]. The grain boundaries enhance conductivity in polycrystalline NiO as they contain a large number of Ni^{2+} vacancies [13]. The volume fraction associated with triple junction falls off sharply for crystallite size greater than 10 nm. This causes an enhanced conductivity for the sample N1. With further increase in size, the grain boundary per unit volume decreases which in turn decreases the number of Ni^{2+} vacancies and hence the conductivity.
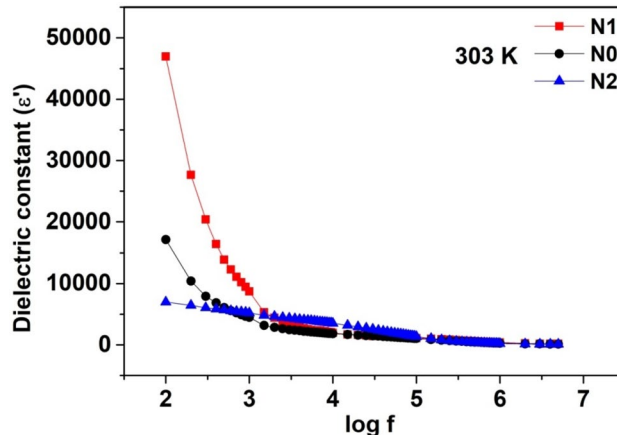
3.3.2 Dielectric studies

The variation of dielectric constant with frequency at room temperature for NiO samples with different crystallite size is portrayed in Fig. 6. The numerical value of ε' is of the order of 10^4–10^3 Hz in the low-frequency regime. The high density of Ni^{2+} vacancies makes nanocrystalline NiO a dielectric material with a high concentration of hopping charge carriers. Such carrier-dominated dielectrics are reported to have a very high value of dielectric constant [35]. This property of NiO can be used as a gate dielectric in metal oxide semiconductor field effect transistor (MOSFET).

The value of ε' is very high in the low-frequency region for all the samples, which decreases rapidly with increase in frequency and becomes almost constant at higher frequencies. The dielectric behaviour of nanostructured materials at low frequencies depends on the excitation of bound electrons, lattice vibrations, dipole orientation and space-charge polarization [36]. The dielectric dispersion curve can be described using Koop's theory [37], which is based on the Maxwell–Wagner model [38]. According to this model, the dielectric structure can be imagined as a system consisting of grains which are highly conducting, separated by

relatively resistive regions called grain boundaries. Under the influence of the electric field, localized accumulation of charges occurs at the grain boundaries which results in interfacial/space charge polarization. The conduction process in NiO is described by the correlated barrier-hopping model (CBH) [13, 38]. CBH model suggests two types of carrier hopping in NiO (i) Inter-well hopping: the hopping of a hole from a Ni^{3+} ion located in one defect potential well to a Ni^{2+} or O^{2-} ion in an adjacent defect potential well and (ii) Intra-well hopping: the hopping of holes between ions within one defect potential well. These holes on reaching the grain boundary get piled up due to its high resistivity, thereby producing space charge polarization. The sharp increase of ε' at low frequency is due to the space-charge polarization caused by impurities and crystal defects [39]. With an increase in frequency, the charge carriers contributing to polarization lag behind the applied field and hence results in a decrease in dielectric constant. Beyond a certain frequency, dipoles are unable to follow the alternating field hence a frequency-independent dielectric behaviour is noticed.

The value of ε' of N1 is higher than that of N0, but falls rapidly for N2. The improved volume fraction of triple junctions in the interfacial region of N0 affects the polarization mechanism, which causes a decrease in its dielectric constant. The disordered structure of the surface, surface energy and Ni^{2+} vacancy distribution of the NiO nanoparticles can affect the value of dielectric constant [40, 41].

The variation of loss tangent $\tan\delta$ with frequency for the samples with different crystallite size at room temperature is shown in Fig. 7. It decreases with increase in frequency and attains a constant value in the high-frequency region for all samples. In nanomaterials, the absorption current produced due to impurities, defects and space charge formation in the interphase layers results in a dielectric loss [42]. The
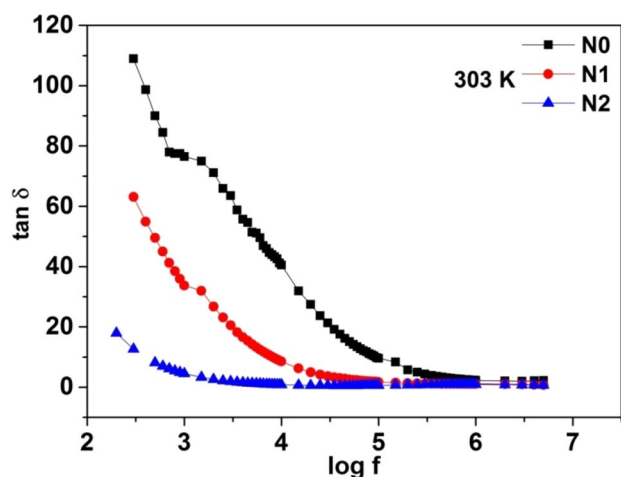
high value of loss tangent at low frequency is due to space charge polarization [43]. The absorption current and hence the dielectric loss gets reduced as the applied frequency increases. With the increase in frequency, the response of dipoles to the changing field decreases and hence the loss tangent approaches a low value.

The maximum value of loss tangent is observed for the sample with the smallest crystallite size. With a decrease in crystallite size, the volume fraction of interfacial regions and grain boundaries and the number of defects that contribute to dielectric loss might increase.

3.3.3 Impedance analysis

The Nyquist plots of the samples N0, N1 and N2 at room temperature and the corresponding equivalent circuit are shown in Fig. 8. Two partially overlapping semicircular arcs are observed at all temperatures which represent two different relaxation mechanisms [44]. The arc at higher frequency represents the contribution of grains and the other in lower frequency is attributed to the grain boundary effects [45]. From the Nyquist plot, it is clear that both grain and grain boundaries are contributing to the physical properties of NiO as offered by Maxwell Wagner model.

The data can be modelled with a circuit consisting of two parallel R-CPE (Constant Phase Element) circuits connected in series. CPE takes into account the frequency dispersion of the capacitance values and the spatial inhomogeneity of the system [46]. The impedance of CPE is of the form $Z_Q = 1/(j\omega)^{\beta}CPE$, where $0 < \beta < 1$. β is a measure of the capacitive nature of the component [44, 47]. An inductor L_s is connected in series with the circuit to account for the electrode contribution. Typical values of the parameters R, C and β, both for grain (R_g, CPE_g, β_g) and grain boundaries (R_{gb}, C_{gb}, β_{gb}) and L_s obtained from the fits are given in Table 3. The grain boundaries are found to be more capacitive and resistive than the grains for all the samples. The value of β (< 1) confirms the non-Debye type of relaxation for all the samples.

3.3.4 AC conductivity

The variation of AC conductivity σ_{ac} with the frequency of the applied field for the samples N0, N1 and N2 at 303 K is illustrated in Fig. 9. The measured AC conductivity for all the samples is found to be much higher than that of single crystalline NiO which is of the order of 10^{-11} S m^{-1} at room temperature. The enhanced AC conductivity is due to the high density of Ni^{2+} vacancies present in the NiO samples [16]. For all samples, σ_{ac} is found to be independent of the applied signal frequency upto about 50 kHz, while at higher frequencies it shows an increasing trend. This frequency independent behaviour at lower frequencies indicates the dominance of DC

Fig. 7 Variation of tan δ with frequency for samples N0, N1 and N2 at 303 K
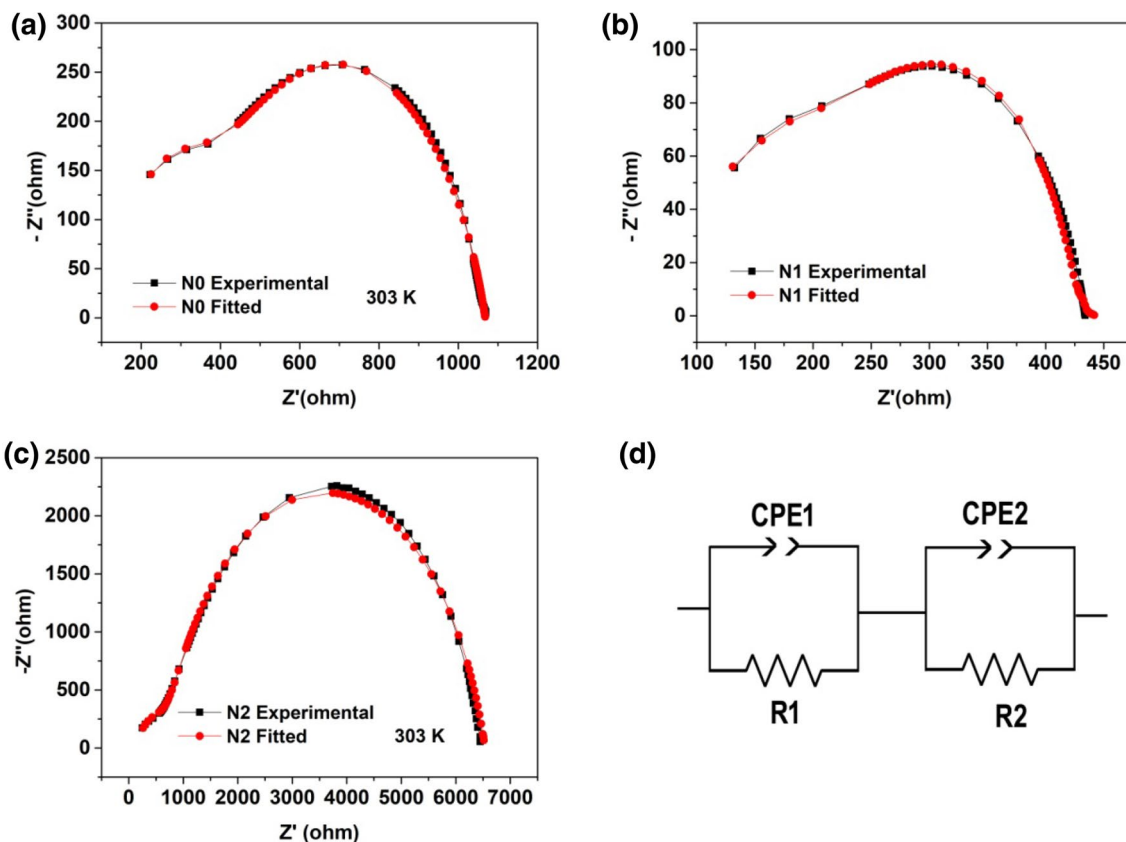
Fig. 8 Nyquist plots of **a** N0, **b** N1, **c** N2 and **d** Equivalent circuit
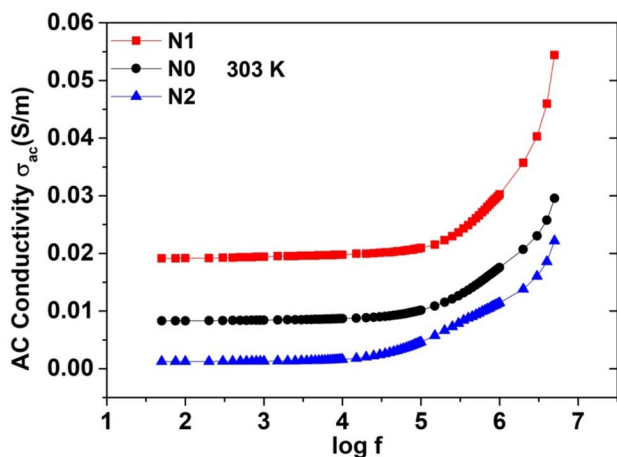
Fig. 9 Variation of σ_{ac} with frequency for samples N0, N1 and N2 at 303 K

conductivity in this region [48]. In the presence of an AC signal, both inter-well and intra-well charge transfer mechanisms suggested by CBH model have a finite probability of occurrence. Several factors such as the energy of the charge carriers, frequency of the applied signal, mean site separation, depth and extent of percolation of the potential wells associated with

Ni^{2+} vacancies influence the relative probabilities of these hopping mechanisms. In the low-frequency region, inter-well hopping which is responsible for DC conduction dominates intra-well hopping [44, 49]. However, as the signal frequency is increased, intra-well hopping probability which contributes to AC conductivity increases. The pumping force that helps in transferring the charge carriers between the different localized states as well as liberating the trapped charges from the different trapping centres increases with frequency [50].

It is found from Fig. 9 that the AC conductivity first increases and then decreases with increase in crystallite size. The variation in the structure of the interfacial region is the reason for the low value of AC conductivity for N0. The value of σ_{ac} of NiO nanoparticles with size < 10 nm depends on the relative volume fractions of the grain boundaries and triple junctions constituting the interfacial region [16]. The decrease in σ_{ac} for N2 is due to the decrease in grain boundary density. According to the correlated barrier-hopping model the AC conductivity,

$$\sigma_{ac} = \frac{\pi^3}{24} N^2 \varepsilon R_\omega^6 \omega \tag{1}$$

where N is the concentration of defect sites contributing to hopping mechanism, ε the dielectric permittivity and R_ω the hopping distance [51, 52]. Calcination increases the grain size and hence decreases the grain boundary density. This, in turn, decreases the value of N which contributes to the AC conductivity of the sample.

3.4 Magnetic properties

The M–H hysteresis curves are plotted at room temperature for NiO nanoparticles with different size as shown in Fig. 10.

The M–H curve for sample N0, with the smallest average crystallite size of 8.2 nm does not have any hysteresis and thus show the property of superparamagnetism with very low retentivity and coercivity. However, the samples N1 and N2 with an average size of 12.4 and 18.5 nm exhibit weak ferromagnetic behaviour with a small hysteresis loop and a low coercive field. The magnetization does not saturate at the highest field of 15 kOe for the samples. Neel suggested that nanoparticles of an antiferromagnetic material will exhibit magnetic properties such as superparamagnetism and weak ferromagnetism [19]. Single crystalline NiO has a rhombohedral structure and is antiferromagnetic below the Neel temperature (573 K) [53]. However, as the grain size is reduced, the surface to volume ratio becomes sufficiently large and the surface effects start to govern the magnetic properties. Because of the structural disorder, the surface spin can be more easily deviated from the antiferromagnetic alignment by a magnetic field. Then the particle can have a nonzero net magnetic moment because of uncompensated spins at the surface. As the particles can have varying size and shape, the magnetic moments will be of different size and they get randomly oriented and interact with each other magnetically [20]. If the size of the grains is further reduced
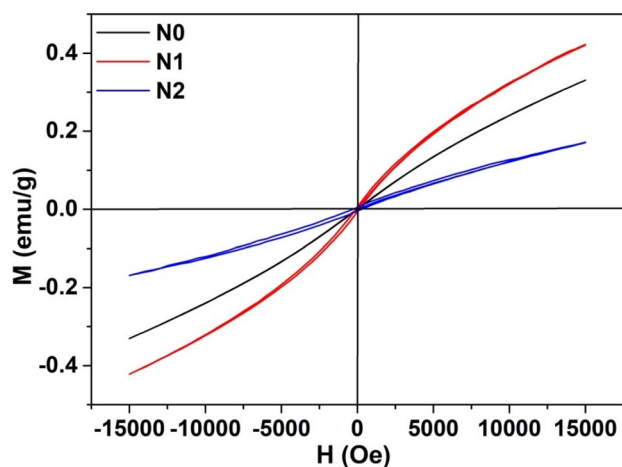
thermal fluctuations will also become an important factor which gives rise to superparamagnetism [54].

The variation in retentivity and coercivity as a function of grain size is depicted in Fig. 11. The superparamagnetic behaviour is reflected in the very low values of coercivity and retentivity for the sample N0. When the particles reach the superparamagnetic size, the energy barrier separating the two energetically degenerate magnetic orientations is small. The thermal activation is then sufficient to switch the magnetic orientation at any temperature. Hence, the coercivity is very small for superparamagnets [55]. With an increase in grain size, the coercivity starts rising as they exhibit ferromagnetic behaviour. This variation of coercivity with grain size can be explained on the basis of domain structure, critical diameter and the anisotropy of the crystal [56, 57]. For small values of grain size, the crystallites prefer to remain as a single domain. Coercivity is found to increase with increasing grain size until a maximum value is reached at the critical diameter corresponding to the transition stage from the single domain to the multi-domain state [58]. The magnetic moment of the individual particle and the magnetic anisotropy energy increases with increase in size, and therefore, stronger field is required for demagnetization. The retentivity is also affected by the grain size. The value increases from a very low value (4.383E−04 emu g^{-1}) for N0, which is superparamagnetic, to a maximum value of 6.170E−03 emu g^{-1} for N1 and then decreases to 4.701E−03 emu g^{-1} for N2. With an increase in grain size the number of grain boundary decreases, thereby decreasing the structural defects and subsequently the value of retentivity [59]. Thus, the magnetic response of nanostructured nickel oxide undergoes significant change due to the surface modification associated with the reduction in grain size. The superparamagnetic property of the sample (N0) can be useful in magnetic biomaterials for magnetic resonance imaging (MRI), cell separation and cell labelling applications [60].

Fig. 10 Magnetic hysteresis of N0, N1 and N2 at room temperature
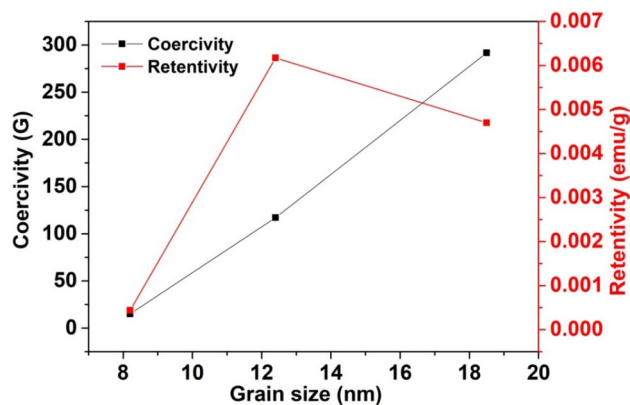
Fig. 11 Variation in magnetic parameters with grain size

4 Conclusion

NiO nanoparticles with crystallite size varying from ~ 8 to 18 nm have been synthesized by calcining the precursor prepared by chemical precipitation method at different temperatures. The W–H plot reveals a decrease in micro-strain with the increase in crystallite size. The observed enhancement in conductivity by several orders of magnitude over that of NiO single crystal is attributed to the high-surface defect density associated with Ni^{2+} vacancies. The dominant effect of the triple junction on the transport properties of NiO nanoparticles with size < 10 nm is clearly established in this study. Complex impedance spectra show two semi-circles, confirming the contribution of grains and grain boundaries to the conductivity. The magnetic behaviour changes from ferromagnetic to superparamagnetic state with the reduction in particle size, which highlights the significance of surface atoms and surface-driven spin rearrangements in shaping the magnetic property of nanocrystalline NiO. The superparamagnetic property of NiO nanoparticles makes it as magnetic biomaterials for biomedical applications.

Data availability The raw/processed data required to reproduce these findings cannot be shared at this time as the data also forms part of an ongoing study.

References

1. C.C. Chen, A.B. Herhold, C.S. Johnson, A.P. Alivisatos, Science **276**, 398 (1997)
2. H.J. Hoffler, R.S. Averback, Scr. Metall. Mater. **24**, 2401 (1990)
3. S. Thota, J. Kumar, J. Phys. Chem. Solids **68**, 1951 (2007)
4. M. Ghosh, K. Biswas, A. Sundaresan, C.N.R. Rao, J. Mater. Chem. **16**, 106 (2006)
5. F. Bodker, M.F. Hansen, C.B. Koch, S. Morup, J. Magn. Magn. Mater. **221**, 32 (2000)
6. P.A. Sheena, H. Hitha, A. Sreedevi, T. Varghese, Mater. Chem. Phys. **229**, 412 (2019)
7. I.S. Lee, N. Lee, J. Park, B.H. Kim, Y.W. Yi, T. Kim, T.K. Kim, I.H. Lee, S.R. Paik, T. Hyeon, J. Am. Chem. Soc. **128**, 10658 (2006)
8. M.A. Nasseri, F. Kamali, B. Zakerinasab, RSC Adv. **5**, 26517 (2015)
9. I. Hotovy, J. Huran, L. Spiess, H. Romanus, D. Buc, R. Kosiba, Thin Solid Films **515**, 658 (2006)
10. F. Cao, G.X. Pan, X.H. Xia, P.S. Tang, H.F. Chen, Electrochim. Acta **111**, 86 (2013)
11. S.A. Needham, G.X. Wang, H.K. Liu, J. Power Sources **159**, 254 (2006)
12. Y.Z. Zheng, M.L. Zhang, Mater. Lett. **61**, 3967 (2007)
13. F.J. Morin, Phys. Rev. B. **93**, 1195 (1954)
14. D. Adler, J. Feinleib, Phys. Rev. B. **2**, 3112 (1979)
15. P. Puspharajah, S. Radhakrishna, J. Mater. Sci. **32**, 3001 (1997)
16. V. Biju, M. Abdul Khader, Mater. Res. Bull. **36**, 5779 (2001)
17. S.A. Makhlouf, M.A. Kassem, M.A. Abdel-Rahim, J. Mater. Sci. **44**, 3438 (2009)
18. C.H. Tsang, R.E. Fontana Jr., T. Lin, D.E. Heim, B.A. Gurney, M.L. Williams, IBM J. Res. Dev. **42**, 103 (1998)
19. L. Néel, in *Low Temperature Physics*, ed. by C. Dewitt, et al. (Gordon and Beach, New York, 1962)
20. S.D. Tiwari, K.P. Rajeev, Phys. Rev. B **72**, 104433 (2005)
21. F. Bodker, M.F. Hansen, C. BenderKoch, S. Morup, J. Magn. Magn. Mater. **221**, 32 (2000)
22. M.A. Khadar, V. Biju, A. Inoue, Mater. Res. Bull. **38**, 1341 (2003)
23. M. Alagiri, S. Ponnusamy, C.J. Muthamizhchelvam, J. Mater. Sci.: Mater. Electron. **23**, 728 (2012)
24. J. Li, R. Yan, B. Xiao, D.T. Liang, D.H. Lee, Energy Fuels. **22**, 16 (2008)
25. T. Nathan, A. Aziz, A.F. Noor, S.R.S. Prabaharan, J. Solid State Electrochem. **12**, 1003 (2008)
26. A.N. Mallika, A.R. Reddy, K.V. Reddy, J. Adv. Ceram. **4**, 123 (2015)
27. B.D. Cullity, S.R. Stock, *Elements of X-ray Diffraction*, 3rd edn. (Prentice Hall, New Jersey, 2001)
28. I. Navas, R. Vinodkumar, K.J. Lethy, M. Satyanarayana, V. Ganeshan, V.P. MahadevanPillai, J. Nanosci. Nanotechnol. **9**, 5254 (2009)
29. G.K. Williamson, W.H. Hall, Acta. Metall. **1**, 22 (1953)
30. K.P. Priyanka, P.A. Sheena, N.A. Sabu, T. George, K.M. Balakrishna, T. Varghese, Ind. J. Phys. **88**, 657 (2014)
31. M.A. Wittenauer, L.L. Van Zandt, Philos. Magn. B **46**, 659 (1982)
32. M. Nachman, L.N. Cojocaru, L.V. Ribco, Phys. Status Solidi **8**, 773 (1965)
33. C. Suryanarayana, Bull. Mater. Sci. **17**, 307 (1994)
34. G. Palumbo, S.J. Thorpe, K.T. Aust, Scr. Metal. Mater. **22**, 1347 (1990)
35. A.K. Jonscher, J. Mater. Sci. **13**, 553 (1978)
36. K.V. Rao, A. SmakulaJ, Appl. Phys. **36**, 2031 (1965)
37. C.G. Koops, Phys. Rev. **83**, 121 (1951)
38. K.W. Wagner, Am. Phys. **40**, 317 (1973)
39. D.P. Snowden, H. Saltzburg, Phys. Rev. Lett. **14**, 497 (1965)
40. V. Biju, M. Abdul Khadar, J. Mater. Sci. **38**, 4058 (2003)
41. B. Jiang, J.L. Peng, L.A. Bursil, W.L. Zhong, IBID **87**, 3462 (2000)
42. K.P. Priyanka, J. Sunny, T. Smitha, E.M. Mohammed, T. Varghese, J. Basic Appl. Phys. **2**, 105 (2010)
43. S. Kamba, V. Bovtun, J. Petzelt, I. Rychetsky, R. Mizaras, A. Brilingas, J. Banys, J. Grigas, M. Kosec, J. Phys.: Condens. Matter **12**, 497 (2000)
44. A. Singh, R. Chatterjee, S.K. Mishra, P.S.R. Krishna, S.L. Chaplot, J. Appl. Phys. **111**, 014113 (2012)
45. B. Gokul, P. Matheswaran, K.M. Abhirami, R. Sathyamoorthy, J. Non-Cryst. Solids **363**, 161 (2013)
46. L.D. Sappia, M.R. Trujillo, I. Lorite, R.E. Madrid, M. Tirado, D. Comedi, P. Esquinazi, Mater. Sci. Eng. B **200**, 124 (2015)
47. V. Varade, G.V. Honnavar, P. Anjaneyulu, K.P. Ramesh, R. Menon, J. Phys. D: Appl. Phys. **46**, 365306 (2013)
48. M. Sayer, A. Mansingh, J.B. Webb, J. Noad, J. Phys. C. **11**, 315 (1978)
49. A.J. Bosman, H.J. Van Daal, Adv. Phys. **19**, 1 (1970)
50. A.M.M. Farea, S. Kumar, K.M. Batoo, A. Yousef, C.G. Lee, Alimuddin. J. Alloys Compd. **464**, 361 (2008)
51. B. Viswanathan, V.R.K. Murthy, *Ferrite Materials Science and Technology* (Narosa Publishing House, New Delhi, 1990)
52. M. George, S.S. Nair, K.A. Malini, P.A. Joy, M.R. Anantharaman, J. Phys. D: Appl. Phys. **40**, 1593 (2007)

53. J.S. Smart, S. Greenwald, Phys. Rev. **82**, 113 (1951)
54. A.G. Kolhatkar, A.C. Jamison, D. Litvinov, R.C. Willson, T.R. Lee, Int. J. Mol. Sci. **14**, 15977 (2013)
55. S. Roy, I. Dubenko, D.D. Edorh, N. Ali, J. Appl. Phys. **96**, 1202 (2004)
56. M. George, A.M. John, S.S. Nair, P.A. Joy, M.R. Anantharaman, J. Magn. Magn. Mater. **302**, 190 (2006)
57. B.D. Cullity, *Introduction to Magnetic Materials* (Addison-Wesley Publishing Company Inc, Reading MA, 1972)
58. M. Sajjia, A. Baroutaji, A.G. Olabi, Ref. Module Mater. Sci. Mater. Eng. (2017). https://doi.org/10.1016/B978-0-12-803581-8.09264-X
59. S.B. Waje, M. Hashim, W.D.W. Yusoff, Z. Abbas, J. Magn. Magn. Mater. **322**, 686 (2010)
60. R.V. Ramanujan, in *Biomedical Materials*, ed. by R. Narayan (Springer Science and Business Media, LLC, Singapore, 2009), p. 477